ARTICLE   OPEN

Check for updates

A two-way photonic quantum entanglement transfer interface

Yiwen Huang[1,6], Yuanhua Li[1,2,6 ✉], Zhantong Qi[1], Juan Feng[1], Yuanlin Zheng[1,3] and Xianfeng Chen[1,3,4,5 ✉]

A quantum interface for two-way entanglement transfer, e.g., between orbital angular momentum degree of freedom in free space and time-energy degree of freedom in optical fibers, provides a way toward establishing entanglement between remote heterogeneous quantum nodes. Here, we experimentally demonstrate this kind of transfer interface by using two interferometric cyclic gates. By using this quantum interface, we perform two-way entanglement transfer for the two degrees of freedom. The results show that the quantum entangled state can be switched back and forth between orbital angular momentum and time-energy degrees of freedom, and the fidelity of the state before and after switching is higher than 90%. Our work demonstrates the feasibility and high performance of our proposed transfer interface, and paves a route toward building a large-scale quantum communication network.

INTRODUCTION

An entanglement-based quantum network is a platform for the science and application of secure communication and distributed quantum computation. In a complex network, quantum entanglement can be encoded in various degrees of freedom (DOF), such as path, polarization, time-energy, and spatial modes. Recently, entanglement of spatial modes, both azimuthal and radial DOF, has especially attracted much attention. Due to the unique phase-intensity profile and unlimited number of orthogonal modes, orbital angular momentum (OAM) entangled states have stimulated a variety of quantum applications[1], such as high-dimensional quantum key distribution[2], quantum teleportation[3], entanglement swapping[4], fundamental tests of quantum mechanics[5], digital spiral imaging[6], and quantum pattern recognition[7]. Currently, OAM entanglement has been more and more widely used in quantum communication tasks. As an important part of two-dimensional transverse space of photons[8], radial modes offer a new platform for many quantum information tasks, such as the fundamental test of quantum mechanics[9] and of high-dimensional entangled states[10], and have potential application in high-dimensional quantum experiment[11]. On the other hand, time-energy entanglement is of great interest as it supports various encodings, including time bins and temporal modes[12–14], and is insensitive to the birefringence effect of fibers[15–17]. Different from polarization entanglement which requires real-time active control to compensate polarization drifts[18–21], time-energy entanglement, both continuous and discrete versions, shows intrinsic robustness for propagation through long-distance fiber with the help of passive dispersion-compensating devices[22,23]. To date, time-energy entanglement sources have been widely used in optical-fiber quantum tasks, such as quantum key distribution[24–26], dense coding[27], and long-distance quantum entanglement swapping[28]. It is an important candidate for building long-distance optical fiber networks.

The future quantum communication network would integrate free space and optical-fiber links[29] and be composed of heterogeneous quantum nodes[19]. In order to accomplish different quantum tasks, the nodes of the network need to transfer the entangled states of information-carrying photons back and forth between different DOF. This requires a reversible quantum entanglement transfer (QET) interface to perfectly perform such a function, which is a key technology for realizing quantum communication between nodes in the network. So far, QET has been implemented from time to polarization[30], polarization to frequency[31], polarization to OAM[32], and path to OAM[33] DOF. Moreover, the integrated interface of OAM beam emitter[34] provides the potential for constructing an integrated network including OAM encoding. Implement of a two-way QET interface that can control quantum entanglement switching back and forth between time-energy and OAM DOF is urgently needed for constructing the large-scale quantum communication network. However, such a two-way QET interface of entangled photons has not been implemented.

Here we demonstrate the experiment of QET between time-energy and OAM DOF of photons. Two interferometric quantum gates consisting of a Franson-type interferemeter with spiral phase plates (SPP) inserted in different paths are utilized for transferring quantum entanglement information from time-energy to OAM DOF. Furthermore, we use two OAM sorters followed by two Mach-Zehnder interferometers (MZIs) to implement QET from OAM to time-energy DOF. The experiment results reveal a high quality of the QET between these two DOF, while preserving quantum coherence and entanglement. Our approach paves the way towards a means of connecting remote heterogeneous quantum nodes in time-energy and OAM subspace.
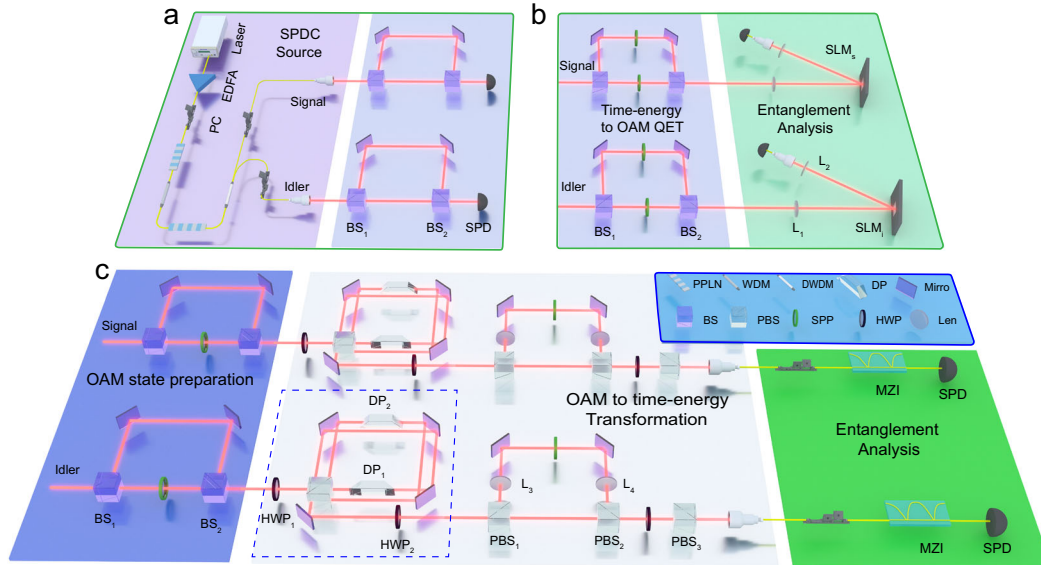
RESULTS

Time-energy entangled source

Our experimental setup is depicted in Fig. 1, where Fig. 1a is the schematic of the experimental setup of spontaneous parametric down-conversion (SPDC) source. A narrow-band continuous-wave laser at 1555.75 nm amplified by an erbium-doped fiber amplifier is frequency doubled in a periodically poled lithium niobate (PPLN) waveguide by second-harmonic generation. The remnant pump laser is suppressed by a wavelength division multiplexing

Fig. 1 Experimental setup. a Schematic of the experimental setup of Spontaneous parametric down-conversion (SPDC) source. Two MZIs serving as a Franson-type interferometer are used to characterize the time entanglement of the photon pairs. **b** Schematic of the experimental setup for characterizing the OAM entanglement. **c** Schematic of the main experimental setup of two-way entanglement transfer. The dashed box indicates the structure of OAM mode sorter which is implemented as a double-path Sagnac interferometer and contains two DPs with a relative angle of 90°. The photon pairs, signal and idler shown in **b** and **c**, are generated by the SPDC source shown in **a**. All the MZIs used in the experiment are steadily phase-locked by piezoelectric transducer systems. EDFA erbium-doped fiber amplifier, WDM wavelength-division multiplexing, DWDM dense wavelength division multiplexing filter, PC polarization controller, L_1 len of $f_1 = 300$ mm, L_2 len of $f_2 = 500$ mm, L_3 and L_4 lens of $f_3 = f_4 = 150$ mm, DP Dove prism, SPP spiral phase plate, HWP half-wave plate, BS 50:50 beam splitter, PBS polarization beam splitter, MZI 1-GHz unbalanced Mach-Zehnder interferometer, SPD single-photon detector (quantum efficiency, $\eta = (10.0 \pm 0.2)\%$; repetition frequency of gate, $f = 50$ MHz; width of gate, 1 ns; dark count probability per nanosecond, $D = 1 \times 10^{-6}$).
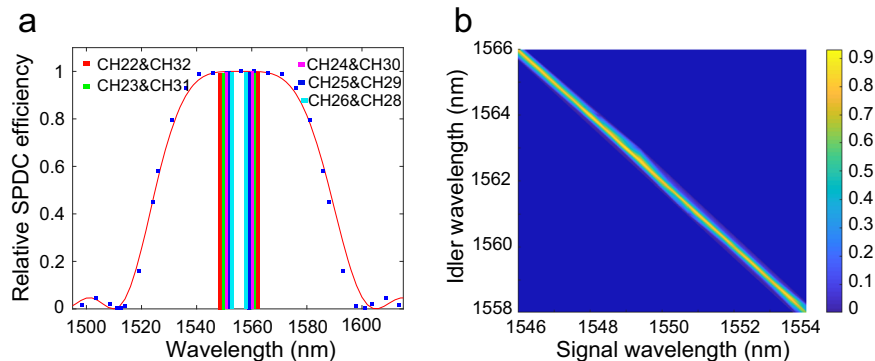
Fig. 2 Spectral characteristics of the SPDC source. a Spectrum of the SPDC source based on PPLN waveguide; the red curve is the theoretical result and the blue square points represent experimental data. The colorful bars indicate the time-energy entangled photon pairs multiplexed by 100-GHz DWDM channels. **b** Joint spectral amplitude of signal and idler photons.

filter with an extinction ratio of 180 dB. The second harmonic is used to generate photon pairs through the type-0 SPDC process in another 5-cm-long PPLN waveguide. Due to the photon energy conservation during the SPDC, the spectrum of the photon pairs is symmetric with respect to the central wavelength of 1555.75 nm and manifests strong frequency correlation, as shown by the SPDC spectrum and joint spectral amplitude in Fig. 2. To measure the joint spectral amplitude, a fiber beam splitter and two tunable Bragg grating filters with a bandwidth of 0.07 nm are used to separate the signal and idler photons. The SPDC source spans a full width at half maximum of approximate 80 nm, covering the whole telecom C- and L-band. We use cascaded 100-GHZ dense wavelength division multiplexing (DWDM) filters to divert the signal and idler photons into 8 standard international telecommunication union channels, i.e., CH22 to CH26 for signal and CH28 to CH32 for an idler.

Firstly, we characterize the time-energy entanglement of the SPDC source by using a Franson-type interferometer[35]. For a SPDC process pumped by a monochromatic continuous-wave laser, one can express the biphoton state at the output of the PPLN waveguide as[23]: $|\psi\rangle = \kappa \int_0^\infty dt \xi(t_i, t_s) \hat{a}_s^\dagger(t_s) \hat{a}_i^\dagger(t_i) |0\rangle$, where $\hat{a}_s^\dagger(t_s)$ and $\hat{a}_i^\dagger(t_i)$ are the creation operators of signal and idler photons, respectively, κ is the coupling constant corresponding to the second-order susceptibility $\chi^{(2)}$ of the PPLN waveguide, and $\xi(t_i, t_s)$ is the time distribution function corresponding to the biphoton coherence time and pump coherence time. Our Franson-type interferometer contains two unequal path-length MZIs with a path delay Δt of 1 ns controlled by a piezo-actuated displacement platform. Considering the temporal coherence time of the signal and idler photons to be $\sigma_{cor} \approx 10$ ps due to the 100-GHZ DWDM filters, such a path delay satisfy the requirement $\tau \gg \Delta t \gg \sigma_{cor}$, where τ is the coherence time of the pump laser. At the output of the Franson-type interferometer, an arrival-time-difference

histogram with three peaks, due to all the possible path combinations, can be recorded by scanning the delay of detect gate of the SPDs. The central peak records the coincidence events that both signal and idler photons simultaneously pass through the long arms or short arms of their corresponding MZIs. The two-photon state combining the OAM freedom in the central peak can be expressed as the following form:

$$|\psi\rangle_0 = \left[\frac{1}{\sqrt{2}}(|t_1\rangle_s|t_1\rangle_i + e^{i(\varphi_s + \varphi_i)}|t_2\rangle_s|t_2\rangle_i)\right] \otimes |0\rangle|0\rangle, \quad (1)$$

where t_1 and t_2 denote the short arm and long arm of the MZIs, φ_s and φ_i are the relative phase between the long arm and short arm of the MZI of signal and idler photons, respectively, and $|0\rangle$ represents that the OAM mode of photon pair is Gaussian mode. In our experiment, another continuous-wave laser at the central wavelength of 1570 nm is injected into the other input port of the beam-splitter as feedback to stabilize the phase of interferometers. This reference laser is offset with SPDC photons on optical paths to avoid extra noise. The two-photon interference fringes under two non-orthogonal phase bases are measured by setting the phase of the MZI in the signal channel at 0 and $\pi/2$ while varying the phase of the idler. The experimental results are shown in Fig. 3. We achieve an average visibility of $V = (95.6 \pm 0.4)\%$, which strongly suggests time-energy entanglement.

QET from time-energy to OAM DOF

In order to deterministically transfer time-energy entanglement to OAM entanglement, SPPs used as mode-shifters are inserted into the two arms of MZIs to form interferometric quantum gates. When a Gaussian photon transmits through the SPP, its azimuthal phase acquires a phase factor $\exp(i\ell\theta)$, and its profile becomes OAM mode of ℓ, where ℓ is an integer and represents the topological charge. After the OAM mode conversion, the photons passing through the short path carry an OAM of $\ell_1\hbar$ when leaving the interferometer, while the OAM of the other becomes $\ell_2\hbar$. After precisely adjusting the relative phase φ_s and φ_i of the two MZIs, one can obtain an OAM entangled state in the central peak as:

$$|\phi^{\pm}\rangle_{OAM} = \frac{1}{\sqrt{2}}(|t_1, \ell_1\rangle_s|t_1, \ell_1\rangle_i \pm |t_2, \ell_2\rangle_s|t_2, \ell_2\rangle_i), \quad (2)$$

where the sign $\pm$ is determined by $\varphi_s + \varphi_i = 0, \pi$. Similarly, the states $|\psi^{\pm}\rangle_{OAM} = \frac{1}{\sqrt{2}}(|t_1, \ell_1\rangle_s|t_1, \ell_2\rangle_i \pm |t_2, \ell_2\rangle_s|t_2, \ell_1\rangle_i)$ can be obtained by inserting SPPs with an OAM mode of ℓ_1/ℓ_2 into the short/long path of the MZI of signal photons and long/short path of the MZI of idler photons, respectively. To show the flexibility and adaptability of this approach, we experimentally
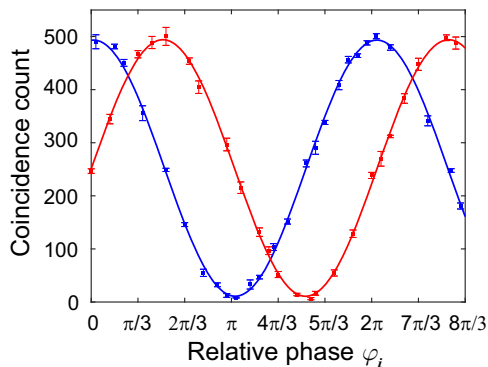
Fig. 3 Two-photon interference fringes for time-energy entanglement before QET. The coincidence counts are recorded by varying the relative phase of MZI of idler photons while the phase of the other is set at 0 (blue line) and $\pi/2$ (red line). Each coincidence count is measured for 10 s. The error bars represent one standard deviation.

construct four maximally entangled states $|\phi^{\pm}\rangle = \frac{1}{\sqrt{2}}(|1\rangle_s|1\rangle_i \pm |-1\rangle_s|-1\rangle_i)$ and $|\psi^{\pm}\rangle = \frac{1}{\sqrt{2}}(|1\rangle_s|-1\rangle_i \pm |-1\rangle_s|1\rangle_i)$. The experimental setup is shown in Fig. 1b. For constructing the states $|\phi^{\pm}\rangle$, two SPPs with an OAM mode of $\ell = 1$ are respectively inserted into the short arms of the MZIs of signal and idler photons while another two SPPs with an OAM mode of $\ell = -1$ are inserted into the long arms. For the states $|\psi^{\pm}\rangle$, SPPs with an OAM mode of $\ell = 1/-1$ are inserted into the short/long arm of the MZI of signal photons and the long/short arm of the MZI of idler photons, respectively. With a diffraction efficiency of high than 98%, the SPPs inserted within two MZIs can effectively convert the Gaussian photons to OAM-carrying photons.

To fully characterize the established OAM states, we perform a quantum state tomography for the four pairs of frequency-correlated channels and reconstruct their density matrices by using the maximum likelihood estimation. Two spatial light modulators (SLM, SLM_s for signal photons, and SLM_i for idler photons) in combination with single-mode fibers and single-photon detectors are used to characterize the OAM entangled states, as shown in Fig. 1b. The SLMs are used to flatten the spiral phase of incident photons and convert them to an Airy-like transverse pattern with most of the intensity in the center, which is efficiently coupled to single-mode fiber. The real and imaginary parts of the reconstructed density matrices ρ are presented in Fig. 4a–d. We calculate the fidelity relative to the ideal Bell states and obtain the average fidelity $F = \langle\psi_{ideal}|\rho|\psi_{ideal}\rangle = (94.1 \pm 1.3)\%$ and purity $P = Tr(\rho^2) = 0.90 \pm 0.01$, as shown in Fig. 4f.

We further measure the two-photon interference fringes to characterize the OAM entangled states. During the measurement, the signal photons are projected onto the states $|D\rangle_s = \frac{1}{\sqrt{2}}(|1\rangle + |-1\rangle)$ and $|L\rangle_s = \frac{1}{\sqrt{2}}(|1\rangle + i|-1\rangle)$ by SLM_s while the idler photons onto $|\theta\rangle_i = \frac{1}{\sqrt{2}}(e^{i\theta}|1\rangle + e^{-i\theta}|-1\rangle)$ by SLM_i. Then, two-photon coincidences are recorded as a function of the rotation angle θ of the phase mask applied to SLM_i. By scanning θ from 0 to 2π, the two-photon interference patterns are obtained, as shown in Fig. 5. The average fringe visibility is calculated to be $V = (93.9 \pm 3.1)\%$, $(93.1 \pm 0.6)\%$, $(94.4 \pm 0.3)\%$, and $(93.8 \pm 0.5)\%$ for the OAM entangled states $|\phi^+\rangle$, $|\phi^-\rangle$, $|\psi^+\rangle$, and $|\psi^-\rangle$, respectively, which exceeds the 71% local bound of the Bell's inequality and strongly suggests the existence of entanglement. To further characterize the entanglement of the prepared state, we measure the S parameter of the Clauser-Horne-Shimony-Holt (CHSH) Bell inequality defined as[36]:

$$S = E(\theta_s, \theta_i) - E(\theta_s, \theta'_i) + E(\theta'_s, \theta_i) + E(\theta'_s, \theta'_i), \quad (3)$$

where $E(\theta_s, \theta_i)$ is expressed as:

$$E(\theta_s, \theta_i) = \frac{C(\theta_s, \theta_i) + C(\theta_s^{\pi/2}, \theta_i^{\pi/2}) - C(\theta_s^{\pi/2}, \theta_i) - C(\theta_s, \theta_i^{\pi/2})}{C(\theta_s, \theta_i) + C(\theta_s^{\pi/2}, \theta_i^{\pi/2}) + C(\theta_s^{\pi/2}, \theta_i) + C(\theta_s, \theta_i^{\pi/2})}.$$

$C(\theta_s, \theta_i)$ represents the coincidence count of signal and idler photons projected onto the state $|\theta_s\rangle_s$ and $|\theta_i\rangle_i$, and $\theta_n^{\pi/2} = \theta_n + \pi/2$ ($n = s, i$). During the experiment, the four angles θ_s and θ_i, θ'_s and θ'_i are set to be 0 and $\pi/8$, $\pi/4$ and $3\pi/8$, respectively[37]. We obtain the result of $S = 2.48 \pm 0.03$, 2.55 ± 0.04, 2.59 ± 0.04, and 2.54 ± 0.05 for the states $|\phi^+\rangle$, $|\phi^-\rangle$, $|\psi^+\rangle$, and $|\psi^-\rangle$, respectively. The experimental results powerfully confirm the quality of the two-photon entanglement in OAM DOF after QET by using such an interferometric gate.

QET from OAM to time-energy DOF

To prove the ability of the two-way QET, we next demonstrate that a two-photon OAM entangled state can be deterministically transferred to time-energy entangled state by using an interferometric cyclic gate. Compared with QET from time-energy to OAM DOF, it is more challenging to coherently convert entanglement
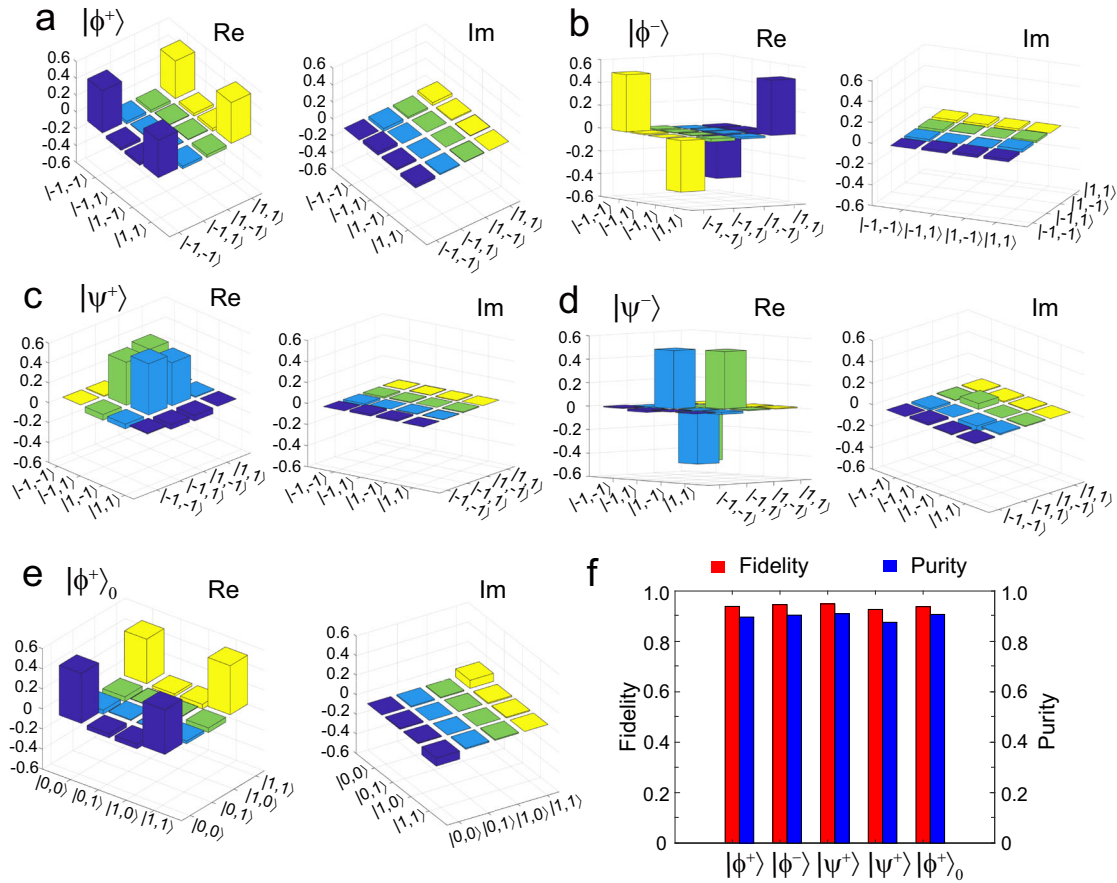
Fig. 4 The measured density matrices, fidelity and purity of the OAM entangled states. a–e The real and imaginary parts of the reconstructed density matrices corresponding to the OAM entangled states $|\phi^+\rangle = \frac{1}{\sqrt{2}}(|1\rangle_s|1\rangle_i + |-1\rangle_s|-1\rangle_i)$, $|\phi^-\rangle = \frac{1}{\sqrt{2}}(|1\rangle_s|1\rangle_i - |-1\rangle_s|-1\rangle_i)$, $|\psi^+\rangle = \frac{1}{\sqrt{2}}(|1\rangle_s|-1\rangle_i + |-1\rangle_s|1\rangle_i)$, $|\psi^-\rangle = \frac{1}{\sqrt{2}}(|1\rangle_s|-1\rangle_i - |-1\rangle_s|1\rangle_i)$ and $|\phi^+\rangle_0 = \frac{1}{\sqrt{2}}(|0\rangle_s|0\rangle_i + |1\rangle_s|1\rangle_i)$, respectively. **f** The measured fidelity and purity from the reconstructed density matrices.

in OAM DOF back to time-energy subspace. The structure of the interferometric cyclic gate is depicted in the OAM to time-energy transformation part of Fig. 1c. The polarization of signal and idler photons is rotated into $\frac{1}{\sqrt{2}}(|H\rangle + |V\rangle)$ by two half-wave plates (HWP) before they enter the interferometric cyclic gates. Then, a double-path Sagnac interferometer containing two DPs is utilized to serve as an OAM sorter to split different OAM modes. Considering that the quantum state of the incident photons is the superposition of two arbitrary OAM modes, ℓ_1 and ℓ_2, the polarizations of photons with different modes will pose perpendicularly to each other[38] once the relative orientation of two DPs is $\alpha = 90°/(\ell_1 - \ell_2)$ (see Methods section for details). In our experiment, we choose the quantum state $|\phi^+\rangle_0 = \frac{1}{\sqrt{2}}(|0\rangle_s|0\rangle_i + |1\rangle_s|1\rangle_i)$ as an example to demonstrate the QET from OAM DOF to time-energy subspace. We firstly prepare the state $|\phi^+\rangle_0$ through QET from time-energy to OAM DOF. A SPP with OAM mode of $\ell = 1$ is inserted in the short path of each MZI of the first Franson-type interferometer, as shown in the OAM state preparation part of Fig. 1c. After reconstructing the density matrix, we obtain the fidelity of 93.8% and state purity of 90.7%, as shown in Fig. 4e and f. To further characterize the entanglement of the prepared state, we measure the S parameter of the CHSH inequality as mentioned above and obtain the result of $S = 2.45 \pm 0.03$, which violates the inequality by 15 standard deviations.

Then, we set the relative orientation of the two DPs in the Sagnac interferometer to be $\alpha = 90°$. At the output of the Sagnac interferometer, the photons of different modes are separated into

different paths by polarization beam splitter 1 (PBS$_1$). Photons with an OAM mode of +1 take the long path, when the others pass through the short path. The two paths are recombined by PBS$_2$, forming an MZI with a delay time of 1 ns. In order to erase any information about OAM profile, a SPP and a 4-f system are inserted in the MZI to convert the OAM photons to the Gaussian mode. Finally, the two-photon state becomes a time-energy entangled state after the erasing of information about polarization and path, then it can be collected into fiber for long distance distribution. We use another Franson-type interferometry consisting of two MZIs with 1-ns relative delay to characterize the generated time-energy entangled state. The experimental results are shown in Fig. 6. We obtain a fitted visibility of $V = (92.1 \pm 0.6)\%$, which strongly suggests time-energy entanglement and implies that the quantum entanglement is coherently transferred into time-energy DOF.

DISCUSSION
The most important feature of our quantum interface is that it maintains the quantum characteristics of the output photons after QET. In our experiment, the entangled state can maintain a high fidelity of over 90% for both QET processes. However, the degradation of the visibility of interference fringes for time-energy entanglement is still non-negligible after QET. This is mainly caused by the imperfection of optical elements, system loss due to non-unity coupling efficiency of space to fiber, and low detection efficiency of SPDs, which can be improved by optimizing system
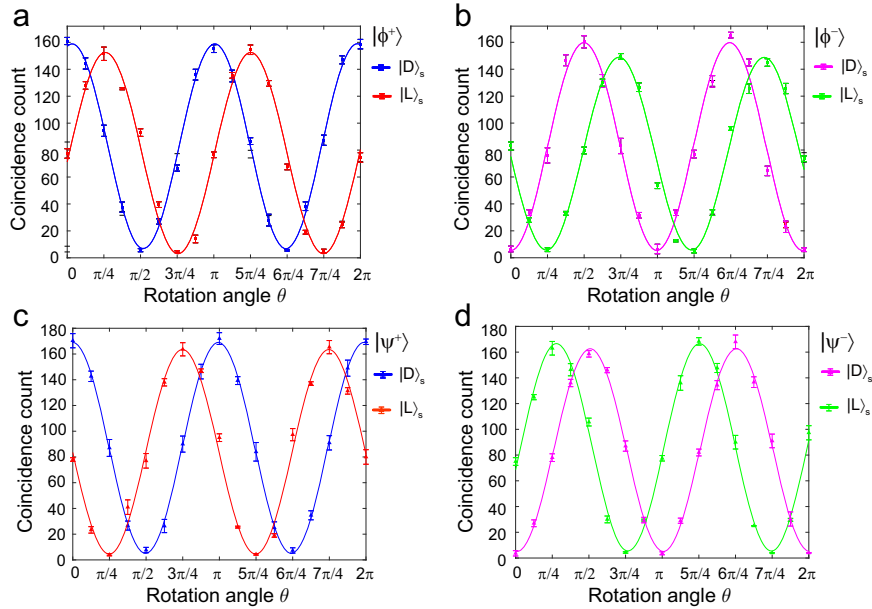
Fig. 5 Two-photon interference fringes of the OAM entangled states. a Interference fringes for the state $|\phi^+\rangle$. **b** Interference fringes for the state $|\phi^-\rangle$. **c** Interference fringes for the state $|\psi^+\rangle$. **d** Interference fringes for the state $|\psi^-\rangle$. Signal photons are projected onto $|D\rangle_s = \frac{1}{\sqrt{2}}(|1\rangle + |-1\rangle)$ and $|L\rangle_s = \frac{1}{\sqrt{2}}(|1\rangle + i|-1\rangle)$, while idler photons are projected onto $|\theta\rangle_i = \frac{1}{\sqrt{2}}(e^{i\theta}|1\rangle + e^{-i\theta}|-1\rangle)$ with θ scanned from 0 to 2π. Each coincidence count is measured for 10 s. The error bars represent one standard deviation.
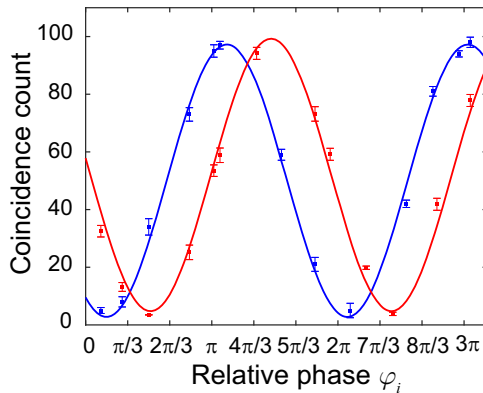
Fig. 6 Two-photon interference fringes for time-energy entanglement after QET. The coincidence counts are recorded by varying the relative phase φ_i of MZI of idler photons while the phase of the signal one is set at $\varphi_s = \pi$ (blue line) and $\varphi_s = 3\pi/2$ (red line). Each coincidence count is measured for 10 s. The error bars represent one standard deviation.

parameters and using a high-performance SPD[39,40]. Another key feature is the high probability of success of entanglement transfer. By taking advantage of the Franson scheme, a deterministic entanglement transfer from time energy to OAM DOF can be theoretically achieved in the central peak of the arrival-time-difference histogram. In our experiment, the probability of success of entanglement conversion is ~96%. As for the other process, due to the high extinction ratio of OAM sorters and the single-mode characteristics of fiber, the QET of OAM back to time-energy DOF is deterministic, too.

On the other hand, our proposed QET interface has the following preponderant characteristics. Firstly, our method paves the way for preparing a multi-channel OAM entangled source by using DWDM technology, which is difficult to implement by directly pumping a nonlinear crystal. In addition, an arbitrary two-dimensional

OAM entangled state can be prepared by replacing the BS_1 in each MZI in the OAM preparation part with a PBS and a HWP. Secondly, the time-energy and OAM DOF belong to high-dimensional Hilbert space. The interferometric cyclic gates can be cascaded with each other to achieve high-dimensional QET, which is promising in high-dimensional quantum tasks. One can prepare the high-dimensional OAM entangled states through QET from time-energy to OAM DOF by inserting relative SPPs into multi-arm unbalanced interferometers. And OAM sorters which split different kinds of OAM, like positive/negative and odd/even OAM, can be cascaded with each other to split high-dimensional OAM modes into different paths. Then one can manipulate the photons of different paths to achieve QET from OAM to time-energy DOF. However, it is more and more challenging to achieve QET from OAM to time-energy DOF as the dimension of the entangled state increases. For the N-dimensional entanglement transfer, $N-1$ OAM sorters are required to split different OAM modes, which significantly increase the complexity and optical loss of the system. Thus, a trade-off between the entanglement dimension and systematic complexity is required when applying the QET in high-dimensional quantum information tasks.

In Summary, we have demonstrated a two-way QET interface with high fidelity between the time-energy and the OAM DOF. Based on this interface, we firstly implement the QET from time-energy to OAM DOF with an average fidelity of the OAM entangled states of higher than 93%. Then, we show quantum entanglement can be coherently tranferred from OAM back to time-energy DOF with a high visibility of Franson-type interference over 92%. This interface can be used to prepare multi-channel OAM entangled sources and paves a way for establishing entanglement between remote heterogeneous quantum nodes. Thus, our scheme has great potential applications in the future quantum communication networks, such as multi-DOF quantum entanglement swapping and quantum direct communication on multinode integrated space-to-fiber communication networks.

METHODS

Scheme of OAM sorter

The OAM sorter is based on a double-path Sagnac interferometer and two embedded Dove prisms, as illustrated in the dashed box in the OAM to time-energy transformation part of Fig. 1c. Assuming that the incoming photons carry an OAM of $\ell\hbar$ and have a horizontal polarization. After passing through the $22.5°$ HWP$_1$, the photon state can be expressed as $\frac{1}{\sqrt{2}}(|H\rangle + |V\rangle) \otimes |\ell\rangle$. When the photons enter the Sagnac interferemeter, they are separated in H and V components by PBS and traverse the embedded Dove prisms, DP$_1$ and DP$_2$, respectively. To effectively separate different OAM photons, one needs to adjust the relative orientation angle a of the two DPs. Due to the Faraday effect, a phase difference of $\exp(i2\ell a)$ is imparted to the two components after they go through the DPs. Finally, the photons recombine in PBS and the following HWP$_2$ convert them to H or V polarization. One can express the output state of photons as:

$$
\begin{aligned}
|\psi\rangle_{out} &\rightarrow |H\rangle \otimes |\ell\rangle \rightarrow \frac{1}{\sqrt{2}}(|H\rangle + |V\rangle) \otimes |\ell\rangle \\
&\rightarrow \frac{1}{\sqrt{2}}(exp(i\ell a)|H\rangle + exp(-i\ell a)|V\rangle) \otimes |\ell\rangle \\
&\rightarrow cos(\ell a)|H\rangle + i sin(\ell a)|V\rangle \otimes |\ell\rangle.
\end{aligned}
\tag{4}
$$

When the orientation angle a is set to be $90°$, the polarization of even and odd OAM photons become H and V, respectively, thus they can be separated by PBS$_1$. Compared with that based on MZI[38], the OAM sorters used in our experiment have the advantage of phase stabilization because the two components have the same optical path in the Sagnac interferometer. If HWP$_1$ and HWP$_2$ are replaced by two quarter wave plates, any two OAM modes, ℓ_1 and ℓ_2, can be separated once the orientation angle are set to be $a = 90°/(\ell_1 - \ell_2)$.

DATA AVAILABILITY

The data that support the plots within this paper and other findings of this study are available from the corresponding author upon reasonable request.

CODE AVAILABILITY

The code that support the plots within this paper and other findings of this study are available from the corresponding author upon reasonable request.

REFERENCES

1. Erhard, M., Fickler, R., Krenn, M. & Zeilinger, A. Twisted photons: new quantum perspectives in high dimensions. *Light Sci. Appl.* **7**, 17146 (2018).
2. Mafu, M. et al. Higher-dimensional orbital-angular-momentum-based quantum key distribution with mutually unbiased bases. *Phys. Rev. A* **88**, 032305 (2013).
3. Wang, X. L. et al. Quantum teleportation of multiple degrees of freedom of a single photon. *Nature* **518**, 516 (2015).
4. Zhang, Y. et al. Simultaneous entanglement swapping of multiple orbital angular momentum states of light. *Nat. Commun.* **8**, 632 (2017).
5. Dada, A. C., Leach, J., Buller, G. S., Padgett, M. J. & Andersson, E. Experimental high-dimensional two-photon entanglement and violations of generalized Bell inequalities. *Nat. Phys.* **7**, 677 (2011).
6. Chen, L., Lei, J. & Romero, J. Quantum digital spiral imaging. *Light Sci. Appl.* **3**, e153 (2014).
7. Qiu, X., Zhang, D., Zhang, W. & Chen, L. Structured-pump-enabled quantum pattern recognition. *Phys. Rev. Lett.* **122**, 123901 (2019).
8. Salakhutdinov, V. D., Eliel, E. R. & Löffler, W. Full-field quantum correlations of spatially entangled photons. *Phys. Rev. Lett.* **108**, 173604 (2012).
9. Chen, L. et al. Realization of the Einstein-Podolsky-Rosen paradox using radial position and radial momentum variables. *Phys. Rev. Lett.* **123**, 060403 (2019).
10. Krenn, M. et al. Generation and confirmation of a (100×100)-dimensional entangled quantum system. *Proc. Natl Acad. Sci. USA* **111**, 6243 (2014).
11. Gu, X., Krenn, M., Erhard, M. & Zeilinger, A. Gouy phase radial mode sorter for light: Concepts and experiments. *Phys. Rev. Lett.* **120**, 103601 (2018).
12. Brecht, B., Reddy, D. V., Silberhorn, C. & Raymer, M. G. Photon temporal modes: a complete framework for quantum information science. *Phys. Rev. X* **5**, 041017 (2015).
13. Maclean, J. P. W., Donohue, J. M. & Resch, K. J. Direct characterization of ultrafast energy-time entangled photon pairs. *Phys. Rev. Lett.* **120**, 053601 (2018).
14. Martin, A. et al. Quantifying photonic high-dimensional entanglement. *Phys. Rev. Lett.* **118**, 110501 (2017).
15. Marcikic, I. et al. Time-bin entangled qubits for quantum communication created by femtosecond pulses. *Phys. Rev. A* **66**, 062308 (2002).
16. Zhang, Q. et al. Distribution of time-energy entanglement over 100 km fiber using superconducting single-photon detectors. *Opt. Express* **16**, 5776–5781 (2008).
17. Grassani, D. et al. Micrometer-scale integrated silicon source of time-energy entangled photons. *Optica* **2**, 88–94 (2015).
18. Treiber, A. et al. A fully automated entanglement-based quantum cryptography system for telecom fiber networks. *New J. Phys.* **11**, 045013 (2009).
19. Yu, L. et al. Two-photon interference at telecom wavelengths for time-bin-encoded single photons from quantum-dot spin qubits. *Nat. Commun.* **6**, 1–10 (2015).
20. Wengerowsky, S., Joshi, S. K., Steinlechner, F., Hübel, H. & Ursin, R. An entanglement-based wavelength-multiplexed quantum communication network. *Nature* **564**, 225–228 (2018).
21. Joshi, S. K. et al. A trusted node-free eight-user metropolitan quantum communication network. *Sci. Adv.* **6**, eaba0959 (2020).
22. Lee, C. et al. Entanglement-based quantum communication secured by nonlocal dispersion cancellation. *Phys. Rev. A* **90**, 062331 (2014).
23. Aktas, D. et al. Entanglement distribution over 150 km in wavelength division multiplexed channels for quantum cryptography. *Laser Photon. Rev.* **10**, 451–457 (2016).
24. Zhong, T. et al. Photon-efficient quantum key distribution using time-energy entanglement with high-dimensional encoding. *New J. Phys.* **17**, 022002 (2015).
25. Zhang, Z., Mower, J., Englund, D., Wong, F. N. C. & Shapiro, J. H. Unconditional security of time-energy entanglement quantum key distribution using dual-basis interferometry. *Phys. Rev. Lett.* **112**, 120506 (2014).
26. Liu, X., Yao, X., Xue, R., Wang, H. & Zhang, W. An entanglement-based quantum network based on symmetric dispersive optics quantum key distribution. *APL Photon.* **5**, 076104 (2020).
27. Williams, B. P., Sadlier, R. J. & Humble, T. S. Superdense coding over optical fiber links with complete Bell-state measurements. *Phys. Rev. Lett.* **118**, 050501 (2017).
28. Li, Y. et al. Multiuser time-energy entanglement swapping based on dense wavelength division multiplexed and sum-frequency generation. *Phys. Rev. Lett.* **123**, 250505 (2019).
29. Chen, Y.-A. et al. An integrated space-to-ground quantum communication network over 4,600 kilometres. *Nature* **589**, 214–219 (2021).
30. Vasconcelos, R. et al. Scalable spin-photon entanglement by time-to-polarization conversion. *npj Quant. Inf.* **6**, 1–5 (2020).
31. Ramelow, S., Ratschbacher, L., Fedrizzi, A., Langford, N. K. & Zeilinger, A. Discrete tunable color entanglement. *Phys. Rev. Lett.* **103**, 253601 (2009).
32. Nagali, E. et al. Quantum information transfer from spin to orbital angular momentum of photons. *Phys. Rev. Lett.* **103**, 013601 (2009).
33. Fickler, R. et al. Interface between path and orbital angular momentum entanglement for high-dimensional photonic quantum information. *Nat. Commun.* **5**, 1–6 (2014).
34. Cai, X. et al. Integrated compact optical vortex beam emitters. *Science* **338**, 363–366 (2012).
35. Franson, J. D. Bell inequality for position and time. *Phys. Rev. Lett.* **62**, 2205 (1989).
36. Clauser, J. F., Horne, M. A., Shimony, A. & Holt, R. A. Proposed experiment to test local hidden-variable theoriesn. *Phys. Rev. Lett.* **23**, 880 (1969).
37. Zhou, Z. Y. et al. Orbital angular momentum-entanglement frequency transducer. *Phys. Rev. Lett.* **117**, 103601 (2016).
38. Zhang, W., Qi, Q., Zhou, J. & Chen, L. Mimicking Faraday rotation to sort the orbital angular momentum of light. *Phys. Rev. Lett.* **112**, 153601 (2014).
39. Marsili, F. et al. Detecting single infrared photons with 93% system efficiency. *Nat. Photon.* **7**, 210–214 (2013).
40. Hu, P. et al. Detecting single infrared photons toward optimal system detection efficiency. *Opt. Express* **28**, 36884–36891 (2020).

AUTHOR CONTRIBUTIONS

X.C. led the project since its conception and supervised all experiments. Y.H. and Y.L. contributed equally to this work. Y.H. and Y.L. under the supervision of X.C. and Y.Z.

performed the experiment and data analysis. Z.Q. and J.F. developed the feedback system for controlling the phase of Mach-Zehnder interferometers. All authors participated in discussions of the results. Y.H., Y.L., and Y.Z. prepared the manuscript with assistance from all other co-authors. All authors have given approval for the final version of the manuscript.

COMPETING INTERESTS

The authors declare no competing interests.

ADDITIONAL INFORMATION

Correspondence and requests for materials should be addressed to Yuanhua Li or Xianfeng Chen.

Reprints and permission information is available at http://www.nature.com/reprints